

# ModTrack: Sensor-Agnostic Multi-View Tracking via Identity-Informed PHD Filtering with Covariance Propagation

Aditya Iyer<sup>1</sup>, Jack Roberts<sup>1</sup>, and Nora Ayanian<sup>1</sup>

<sup>1</sup>Department of Computer Science, Brown University, Providence, RI, USA,  
{aditya\_iyer, jack\_roberts, nora\_ayanian}@brown.edu

## Abstract

Multi-View Multi-Object Tracking (MV-MOT) aims to localize and maintain consistent identities of objects observed by multiple sensors. This task is challenging, as viewpoint changes and occlusion disrupt identity consistency across views and time. Recent end-to-end approaches address this by jointly learning 2D Bird’s Eye View (BEV) representations and identity associations, achieving high tracking accuracy. However, these methods offer no principled uncertainty accounting and remain tightly coupled to their training configuration, limiting generalization across sensor layouts, modalities, or datasets without retraining. We propose ModTrack, a modular MV-MOT system that matches end-to-end performance while providing cross-modal, sensor-agnostic generalization and traceable uncertainty. ModTrack confines learning methods to just the *Detection and Feature Extraction* stage of the MV-MOT pipeline, performing all fusion, association, and tracking with closed-form analytical methods. Our design reduces each sensor’s output to calibrated position-covariance pairs  $(\mathbf{z}, R)$ ; cross-view clustering and precision-weighted fusion then yield unified estimates  $(\hat{\mathbf{z}}, \hat{R})$  for identity assignment and temporal tracking. A feedback-coupled, identity-informed Gaussian Mixture Probability Hypothesis Density (GM-PHD) filter with HMM motion modes uses these fused estimates to maintain identities under missed detections and heavy occlusion. ModTrack achieves 95.5 IDF1 and 91.4 MOTA on *WildTrack*, surpassing all prior modular methods by over 21 points and rivaling the state-of-the-art end-to-end methods while providing deployment flexibility they cannot. Specifically, the same tracker core transfers unchanged to *MultiviewX* and *RadarScenes*, with only perception-module replacement required to extend to new domains and sensor modalities.

**Keywords:** Multi-view tracking, Sensor-agnostic fusion, Uncertainty propagation, Random finite sets

## 1 Introduction

Multi-view multi-object tracking (MV-MOT) underpins applications from surveillance to collaborative robotics. This task is challenging because objects observed from different viewpoints vary significantly in appearance, scale, and visibility, while occlusion and missed detections disrupt identity consistency across both views and time.

Recent end-to-end approaches [20, 25, 21, 22] achieve high accuracy by jointly learning Bird’s Eye View (BEV) representations and data association, but they provide no interpretable uncertainty estimates and remain tightly coupled to the sensor configuration seen during training, making adaptation to new sensors or modalities difficult without retraining or architectural modification.

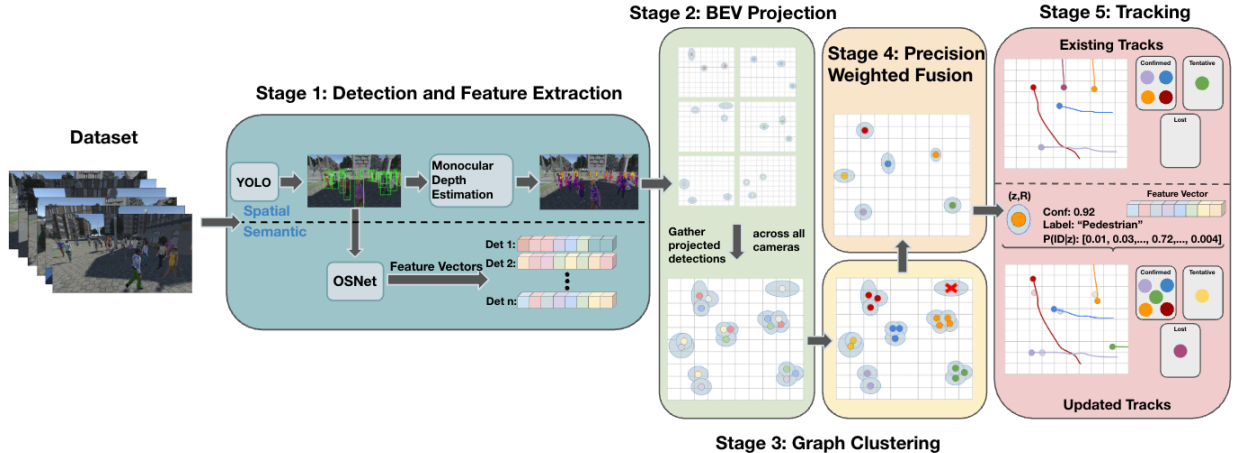


Figure 1: **ModTrack pipeline.** Per-camera detections and appearance features (Stage 1) are projected to BEV with Jacobian-propagated covariance (Stage 2), associated via  $\chi^2$  graph clustering (Stage 3), and precision-weighted into fused  $(\hat{\mathbf{z}}, \hat{\mathbf{R}})$  pairs (Stage 4). An identity-informed GM-PHD filter (Stage 5) maintains persistent identities, with track predictions feeding back to guide identity assignment (dashed). Neural modules (blue) are confined to Stage 1; all downstream stages are purely analytical.

Classical random finite set (RFS) filters provide principled multi-target estimation with closed-form covariance propagation [23]. However, the standard PHD filter does not maintain persistent identities. Labeled extensions [24] recover identities but require combinatorial hypothesis enumeration, and existing multi-view RFS trackers operate in image-space bounding boxes rather than calibrated BEV coordinates, preventing metric covariance propagation for cross-camera fusion and limiting performance in dense tracking scenarios [14].

We propose ModTrack, a modular MV-MOT system that rivals end-to-end accuracy while providing interpretable, traceable uncertainty, by confining learning to just the *Detection and Feature Extraction* stage of the pipeline (Figure 1) and performing all fusion, association, and tracking with closed-form analytical methods. The tracking backend uses the GM-PHD predict-update recursion as the backbone for state estimation and component management, augmented with identity-assignment and lifecycle heuristics; We use the term *identity-informed* GM-PHD to distinguish this method from the standard unlabeled recursion, and treat it as a practically motivated adaptation of PHD filtering. ModTrack adapts to new sensor configurations at inference time seamlessly, avoiding the retraining or engineering accommodations typically required by end-to-end approaches. It also extends prior RFS trackers by operating directly in calibrated BEV space with metric covariance propagation, narrowing the accuracy gap to learned methods in high-clutter scenes. Across domains, all sensor measurements are represented as calibrated position-covariance pairs  $(\mathbf{z}, \mathbf{R})$ , so the same analytical core runs unchanged on WildTrack [6] (7 real cameras), MultiviewX [11] (6 synthetic cameras), and RadarScenes [19] (4 automotive radars), requiring only perception-module replacement. On WildTrack, ModTrack achieves 95.5 IDF1 and 91.4 MOTA, surpassing all prior modular methods by over 21 points and rivaling state-of-the-art end-to-end methods.

The contributions of this work are threefold.

1. **Identity-informed GM-PHD filter with closed-loop propagation.** We augment the GM-PHD filter with persistent identity labels, HMM motion modes, and appearance features. Track predictions feed back as association priors into each PHD update, yielding a +8.9 IDF1 gain

over spatial information-only association.

2. **Analytical covariance chain.** A fully interpretable uncertainty pipeline propagates monocular depth variance through Jacobian BEV projection,  $\chi^2$ -calibrated graph clustering, and common-mode-aware precision-weighted fusion, with every covariance traceable to physical sensor characteristics.
3. **Sensor-agnostic deployment flexibility.** The identical tracker core operates unchanged on WildTrack, MultiviewX, and RadarScenes with only perception-module replacement, and we validate robustness to sensor dropout over all  $\binom{7}{k}$  camera subsets of WildTrack.

## 2 Related Work

**End-to-End and Learned Multi-View Tracking.** Early multi-camera systems [7] tracked objects independently per camera and reconciled identities across views using appearance cues and epipolar constraints. Learned

re-identification embeddings improved cross-view matching [32, 26]. More recent approaches perform joint reasoning directly in BEV. EarlyBird [20] projects per-camera features to a shared ground plane before joint detection and tracking, while later work introduces hierarchical graph reasoning (MCBLT [25]), sparse cross-view transformers (SCFusion [22]), view-aware attention mechanisms [2], and trajectory-level motion–appearance aggregation (MVTrajecter [27], TrackTacular [21]). Related formulations treat multi-view association as a learned graph problem (UMPN [9]) or support variable camera configurations for BEV detection (MIC-BEV [31]). Despite strong performance, these methods typically embed sensor geometry and fusion within learned parameters and do not expose explicit uncertainty estimates.

**Random Finite Set Tracking.** Random finite set (RFS) formulations provide a principled Bayesian framework for multi-target estimation under clutter and missed detections. The GM-PHD filter [23] offers closed-form multi-target state estimation with linear complexity in the number of mixture components, but does not maintain persistent identity labels. The GLMB filter [24] restores labeled tracking with full Bayesian data association, yet requires enumerating association hypotheses whose number grows combinatorially. The LMB filter [17] offers a tractable approximation but, like GLMB, carries only statistical labels without appearance integration or feedback from track state to measurement assignment. MV-GLMB-OC [14] extends GLMB to MV-MOT in pedestrian settings, incorporating occlusion reasoning across cameras, but operating in image-space bounding boxes and is unable to propagate metric covariances in a unified world frame. While RFS-based methods provide rigorous uncertainty handling, they have not been combined with BEV-based geometric fusion or scalable identity reasoning as used in contemporary learned MV-MOT systems.

ModTrack bridges learned BEV-based tracking and classical RFS filtering. By combining precision-weighted multi-view fusion with an RFS-style identity-informed GM-PHD backend, it preserves explicit probabilistic state estimates while remaining competitive with modern learned MV-MOT systems.

## 3 Methodology

### 3.1 Detection and Feature Extraction

ModTrack’s detection and feature extraction stage is sensor-agnostic: any front-end that produces calibrated BEV position-covariance pairs  $(\mathbf{z}, R)$  can drive the identical downstream tracking pipeline. We describe two perception modules in this work, a monocular vision front-end and an analytical radar front-end, to validate this claim across modalities.

#### 3.1.1 Camera Front-End (WildTrack, MultiviewX).

At each time step,

YOLOv11x [12] predicts bounding boxes, class labels, and confidence scores for each camera. For each detection, we estimate metric depth by precision-weighting two complementary geometric cues: a ground-plane footprint back-projection and a bounding-box height prior under the pinhole camera model. A learned monocular depth network [15] serves as an outlier check, inflating the fused variance when it confidently disagrees with the geometric estimate. The resulting depth  $\hat{d}$  and variance  $\sigma_d^2$  are passed to the BEV projection stage (Section 3.2); full derivations and parameter choices are provided in Appendices A and F, respectively.

OSNet-AIN [34] then processes each bounding box and computes feature vectors for each detection. These serve as appearance/semantic identity cues used to augment the PHD filter.

#### 3.1.2 Radar Front-End (RadarScenes).

Each radar measurement provides range  $r$  and azimuth  $\theta$  with known uncertainties  $(\sigma_r, \sigma_\theta)$ , where  $\theta$  is measured from the forward (longitudinal) sensor axis so that  $x_s = r \sin \theta$  and  $y_s = r \cos \theta$  in the sensor-local frame. The Jacobian of this polar-to-Cartesian transform,

$$J_{\text{radar}} = \begin{bmatrix} \sin \theta & r \cos \theta \\ \cos \theta & -r \sin \theta \end{bmatrix}, \quad (1)$$

yields sensor-local Cartesian covariance  $R_s = J_{\text{radar}} \text{diag}(\sigma_r^2, \sigma_\theta^2) J_{\text{radar}}^\top$ . A rotation  $R_\psi$  (ego-vehicle yaw plus sensor mount angle) transforms to the global BEV frame:

$$R_{\text{BEV}} = R_\psi R_s R_\psi^\top + R_{\text{pose}}, \quad (2)$$

Object class and confidence scores are derived from Doppler velocity and radar cross-section via ad-hoc thresholds, replacing YOLO with zero learned parameters. DBSCAN pre-clustering [10] groups per-point detections into object-level measurements. This produces the same  $(\mathbf{z}, R)$  interface without any semantic information.

### 3.2 Ground-Plane Projection with Jacobian Uncertainty Propagation

This subsection applies to the camera front-end (Section 3.1); the radar front-end (Section 3.1.2) produces  $(\mathbf{z}, R)$  pairs directly and bypasses ground-plane projection.

Given a detection at pixel  $(u, v)$  in camera  $c$  with estimated depth  $\hat{d}$  and variance  $\sigma_d^2$ , we back-project  $\mathbf{r}_c = K^{-1}[u, v, 1]^\top$ , map the ray in the camera frame into the world frame at the depth  $\hat{d}$ , and orthogonally project it onto the ground plane:

$$\mathbf{X}_w = R_c(\hat{d}\mathbf{r}_c) + \mathbf{t}_c, \quad \mathbf{X}_{\text{proj}} = \mathbf{X}_w + \left(d_{\text{plane}} - \mathbf{n}^\top \mathbf{X}_w\right) \mathbf{n}, \quad (3)$$

and define the BEV position  $\mathbf{z}_{\text{BEV}} = \mathbf{X}_{\text{proj}, 1:2}$ .

We then propagate the scalar depth uncertainty through the projection using the Jacobian with respect to  $\hat{d}$ , producing a rank-1 BEV covariance term  $R_{\text{depth}} = \sigma_d^2 J J^\top$ . The full derivation, including the closed-form Jacobian and the role of the horizontal-plane assumption, is given in Supplementary Material (Supp. Material) A.1. We model the BEV measurement covariance as the sum of the depth-propagated term and an isotropic calibration/ego-pose term,  $R_{\text{BEV}} = R_{\text{depth}} + R_{\text{pose}}$ , where  $R_{\text{pose}} = \sigma_{\text{pose}}^2 I_2$  and  $\sigma_{\text{pose}}$  is set per dataset (Supp. Material Table 6); Supp. Material A.1 gives the eigenvalue flooring used to avoid overconfident gating. This defines the *sensor-agnostic*  $(\mathbf{z}, R)$  interface for the camera front-end.

### 3.3 $\chi^2$ Graph Clustering

In order to group  $(\mathbf{z}, R)$  pairs from different sensors associated with the same object we construct an association graph where edge weights encode the  $\chi^2$  consistency (survival) probability that two detections originate from the same target. For detections  $p_i$  and  $p_j$  from distinct sensors, the Mahalanobis distance under summed covariances is

$$d_{ij}^2(p_i, p_j) = (\mathbf{z}_i - \mathbf{z}_j)^\top (R_i + R_j)^{-1} (\mathbf{z}_i - \mathbf{z}_j). \quad (4)$$

Under the null hypothesis that both observations originate from the same physical location,  $d_{ij}^2$  follows a  $\chi^2$  distribution with 2 degrees of freedom. The resulting  $\chi^2$  consistency score is  $P_{\text{same}}(p_i, p_j) = 1 - F_{\chi^2_2}(d_{ij}^2)$ , where  $F_{\chi^2_2}$  is the  $\chi^2$  CDF. Edges with  $P_{\text{same}} > \tau_P$  (corresponding to the  $\chi^2_{2,0.99}=9.21$  gate at  $\tau_P=0.01$ ) are retained; a hard Euclidean cutoff  $\tau_{\text{euc}}$  prevents transitive chaining. Following ByteTrack-style [30] cascaded confidence processing, we first cluster high-confidence estimations, then cluster low-confidence estimations in a second pass only for tracks left unmatched after the first pass. Because transitive closure can place multiple estimates from the same sensor into one component, we additionally split each estimate into sensor-unique groups (at most one estimate per sensor, selecting higher-confidence estimates first) before downstream fusion. This is based on the assumption that the object detector does not produce duplicate detections for a single object. We retain only connected components supported by at least two distinct sensors; singleton components are discarded before fusion.

### 3.4 Precision-Weighted Multi-View Fusion

For each cluster with  $M$  sensor measurements  $\{(\mathbf{z}_m, R_m)\}_{m=1}^M$ , we decompose each covariance into an independent term and a shared common-mode term (calibration/ego-pose),  $R_m = R_{\text{indep},m} + R_{\text{pose}}$ , and fuse only the independent components (when the shared term is available and consistent across measurements; otherwise  $R_{\text{pose}}=0$ ):

$$P_{\text{indep}}^{-1} = \sum_{m=1}^M R_{\text{indep},m}^{-1}, \quad (5)$$

$$\hat{\mathbf{z}}_{\text{fused}} = P_{\text{indep}} \sum_{m=1}^M R_{\text{indep},m}^{-1} \mathbf{z}_m, \quad (6)$$

$$P_{\text{fused}} = P_{\text{indep}} + R_{\text{pose}}. \quad (7)$$

The fused estimate  $(\hat{\mathbf{z}}, \hat{R}) \triangleq (\hat{\mathbf{z}}_{\text{fused}}, P_{\text{fused}})$  remains order-independent; importantly, only the independent perceptual uncertainty shrinks with additional sensors, while the shared calibration/ego-pose term is added back once and therefore does not spuriously vanish. A confidence-weighted appearance feature is pooled across cluster members when semantic information is available:

$$\mathbf{f}_{\text{c}} = \frac{\sum_{m=1}^M \beta_m \cdot \hat{\mathbf{f}}_m}{\left\| \sum_{m=1}^M \beta_m \cdot \hat{\mathbf{f}}_m \right\| + \epsilon}, \quad (8)$$

where  $\hat{\mathbf{f}}_m = \mathbf{f}_m / \|\mathbf{f}_m\|$  is the  $L_2$ -normalized appearance feature and  $\beta_m$  is the detection confidence.

### 3.5 Identity-Informed GM-PHD Filter and Closed-Loop Identity Assignment

#### 3.5.1 GM-PHD State Definition and Tracking Loop.

We build on the GM-PHD predict-update recursion [23] as the backbone for state estimation and component management, augmenting it with persistent identity labels, appearance features, HMM motion modes, and lifecycle heuristics for practical identity maintenance. These pragmatic extensions prioritize robust identity tracking over strict adherence to the RFS-theoretic PHD recursion. The  $j$ -th Gaussian component at time step  $k$  is:

$$\mathcal{C}_k^{(j)} = \{w_k^{(j)}, \mathbf{m}_k^{(j)}, P_k^{(j)}, \text{ID}_k^{(j)}, s_k^{(j)}, \mathbf{f}_k^{(j)}\}, \quad (9)$$

where  $w$  is the PHD weight,  $\mathbf{m} = [x, y, \dot{x}, \dot{y}]^\top$  is the BEV state,  $P \in \mathbb{R}^{4 \times 4}$  is the state covariance, ID is the persistent identity,  $s \in \{1, 2, 3\}$  is the HMM motion mode, and  $\mathbf{f}$  is the pooled appearance feature.

We distinguish between *components* and *tracks*: a component  $j$  is a single Gaussian hypothesis (typically corresponding to one motion-mode hypothesis), while a track  $t$  denotes a persistent identity label and may be represented by multiple components  $\mathcal{J}_k(t) \triangleq \{j : \text{ID}_k^{(j)} = t\}$  within a frame.

At each frame, the method follows the same loop: (i) export one representative GM-PHD component state per track to the fusion stage, (ii) assign each fused cluster both a hard identity and a soft identity distribution using that exported pool, (iii) predict the existing GM-PHD components forward by one time step and append identity-informed birth components, (iv) perform track-level association and Kalman update, and then (v) prune, merge, and apply lifecycle transitions before exposing the next frame’s track pool.

#### 3.5.2 Closed-Loop Identity Prior.

The fusion stage and the PHD filter communicate in a *closed loop*. Before processing new measurements, the filter exports one representative component per visible track,  $\mathcal{T}_k = \{(t, \mathbf{m}_k^{(j_t^*)}, P_k^{(j_t^*)}, s_k^{(j_t^*)}, \mathbf{f}_k^{(j_t^*)})\}_{t=1}^{T_k}$ , where  $j_t^* = \arg \max_{j \in \mathcal{J}_k(t)} w_k^{(j)}$ . For each fused estimate ( $\hat{\mathbf{z}}_i, \hat{R}_i$ ) and representative component  $t$ , a gated Mahalanobis cost drives Hungarian matching [13]:

$$\text{Cost}_{i,t} = \begin{cases} d_{i,t}^2, & d_{i,t}^2 < \tau_{\text{gate}} \\ +\infty, & \text{otherwise} \end{cases}, \text{Cost}_{\text{new}} = \tau_{\text{new}} \quad (10)$$

Here  $d_{i,t}^2$  is computed as in Equation (4) with  $p_i \triangleq (\hat{\mathbf{z}}_i, \hat{R}_i)$  and  $p_t \triangleq (\mathbf{z}_t, R_t)$ , where  $(\mathbf{z}_t, R_t)$  is the predicted BEV position and covariance from the  $\mathbf{m}, P$  entries of the representative component for track  $t$ .

A heuristic spatial identity score provides a soft preference toward nearby tracks. Rather than a full Bayesian posterior, we apply the same  $\chi_2^2$  gate as Equation (10): the soft distribution is formed only over tracks with  $d_{i,t}^2 < \tau_{\text{gate}}$  and then renormalized:

$$g_{i,t} = \exp\left(-\frac{d_{i,t}^2}{2\sigma_{\text{spatial}}^2}\right), \quad \pi_{i,t}^{\text{geo}} = \frac{\exp(g_{i,t}/\tau_{\text{geo}})}{\sum_{t'} \exp(g_{i,t'}/\tau_{\text{geo}})}. \quad (11)$$

where  $\sigma_{\text{spatial}} = 1.0$  is a fixed spatial bandwidth and  $\tau_{\text{geo}}$  controls the sharpness of the softmax.  $\pi_{i,t}^{\text{geo}}$  denotes a normalized spatial proximity score for assigning measurement  $i$  to track  $t$ . The hard Hungarian identity initializes the candidate persistent label for the fused cluster, while the soft distribution re-enters the tracker through the association cost in Equation (17). The Hungarian-assigned identity receives nonzero mass before renormalization, to ensure each measurement provides a valid distribution.

### 3.5.3 Prediction and Identity-Informed Birth.

Three motion modes share the linear state-transition structure  $\mathbf{x}_{k+1} = F_s \mathbf{x}_k + \mathbf{w}_k$  with  $\mathbf{w}_k \sim \mathcal{N}(0, Q_s)$ : *stationary* ( $s=1$ ) damps velocity, *constant velocity* ( $s=2$ ) uses the standard CV transition, and *maneuvering* ( $s=3$ ) uses the same transition with elevated process noise  $Q_3 \gg Q_2$  [5]. Mode transitions follow a class-specific Markov chain  $\Pi_{ij}^{(c)} = P(s_{k+1}=j \mid s_k=i)$ .

Prediction and birth are executed as a single stage. We first propagate the surviving components through the HMM motion model,

$$w_{k|k-1}^{(j,s')} = p_S^{(c)} \cdot \Pi_{s_k^{(j)},s'}^{(c)} \cdot w_k^{(j)}, \quad (12)$$

$$\mathbf{m}_{k|k-1}^{(j,s')} = F_{s'} \mathbf{m}_k^{(j)}, \quad (13)$$

$$P_{k|k-1}^{(j,s')} = F_{s'} P_k^{(j)} F_{s'}^\top + Q_{s'}^{(c)}. \quad (14)$$

and then append identity-aware birth components from the current fused clusters whose hard identity assignment does not match an existing predicted track and whose confidence exceeds the birth threshold  $\tau_{\text{birth}}$ ,

$$\mathbf{m}_{\text{birth}}^{(s)} = \begin{bmatrix} \hat{\mathbf{z}}_{\mathcal{C}} \\ \mathbf{0} \end{bmatrix}, \quad P_{\text{birth}}^{(s)} = \begin{bmatrix} \hat{R}_{\mathcal{C}} & \mathbf{0} \\ \mathbf{0} & (\sigma_v^{(c)})^2 I_2 \end{bmatrix}, \quad w_{\text{birth}}^{(s)} = \beta_{\text{max}} \cdot \bar{\Pi}_{1,s}, \quad (15)$$

where  $\sigma_v^{(c)}$  is the class-specific birth velocity prior,  $\bar{\Pi}_{1,\cdot}$  is the stationary-mode prior, and  $\beta_{\text{max}}$  is the maximum detection confidence in the cluster. Multiple mode hypotheses are retained through association and update, then collapsed during post-update component management.

### 3.5.4 Track-Level Association and Update.

At this point, the predicted pool contains both propagated hypotheses from existing tracks and newly initialized tentative birth hypotheses. These predicted components are associated against the current fused measurements from the same frame. Association is performed at the *track level* rather than the component level so that multiple HMM modes of the same identity do not compete for different measurements within the same frame.

**Cost construction.** For each track component  $j$  and measurement  $i$ , the base cost is the Gaussian negative log-likelihood:

$$c_{ij}^{\text{base}} = \frac{1}{2} (d_{ij}^2 + \log |S_k^{(j,i)}|) - \log p_D^{(c)}, \quad (16)$$

where  $d_{ij}^2 = (\mathbf{z}_k^{(i)} - H \mathbf{m}_{k|k-1}^{(j)})^\top (S_k^{(j,i)})^{-1} (\mathbf{z}_k^{(i)} - H \mathbf{m}_{k|k-1}^{(j)})$  and  $S_k^{(j,i)} = H P_{k|k-1}^{(j)} H^\top + R_k^{(i)}$  is the innovation covariance ( $H=[I_2 \mid 0]$ ). We omit the constant  $\log(2\pi)$  term, since it is a fixed offset on all match costs but would otherwise distort match-vs-miss

comparisons. Pairs failing the same  $\chi_2^2$  gate as Section 3.3 are treated as infeasible ( $c_{ij} = +\infty$ ). Three additional terms modify the cost:

$$c_{ij} = c_{ij}^{\text{base}} - \lambda_{\text{assoc}} \cdot \pi_{i,t}^{\text{geo}} - \mu_{\text{sem}} \cdot \cos(\mathbf{f}_k^{(j)}, \mathbf{f}_k^{(i)}) + \psi_{\text{turn}}(j, i), \quad (17)$$

where  $\lambda_{\text{assoc}}$  is the identity boost,  $\mu_{\text{sem}}$  is the appearance similarity boost, and  $\psi_{\text{turn}}$  is a speed-adaptive turn penalty.

**Track-level grouping.** Components are grouped by identity; for each track  $t$  and measurement  $i$ , the grouped cost is  $c_{t,i} = \min_{j \in \mathcal{J}_k(t)} c_{ij}$ . We then solve a gated track-level Hungarian assignment over the confirmed-track subset, while tentative/lost hypotheses (including newly birthed tracks) are updated from the remaining measurements in a second pass; the full augmented assignment matrix and second-pass details are given in Supp. Material B.

Given the resulting assignments, matched components receive a Kalman update:

$$K_k^{(j,i)} = P_{k|k-1}^{(j)} H^\top (S_k^{(j,i)})^{-1}, \quad (18)$$

$$\mathbf{m}_k^{(j)} = \mathbf{m}_{k|k-1}^{(j)} + K_k^{(j,i)} (\mathbf{z}_k^{(i)} - H \mathbf{m}_{k|k-1}^{(j)}), \quad (19)$$

$$P_k^{(j)} = (I - K_k^{(j,i)} H) P_{k|k-1}^{(j)} (I - K_k^{(j,i)} H)^\top + K_k^{(j,i)} R_k^{(i)} K_k^{(j,i)\top}. \quad (20)$$

These matched components also receive a weight boost  $w \leftarrow \min(w + w_{\text{boost}}, 1)$ ; unmatched components receive a miss penalty  $w \leftarrow w \cdot (1 - p_D)$  and are not updated.

### 3.5.5 Component Management and Track Lifecycle.

After the PHD update, low-weight components are pruned, nearby components with the same identity may be merged, and only the dominant motion-mode component is retained per identity, yielding one representative component per identity for the next frame.

Tracks evolve through TENTATIVE, CONFIRMED, and LOST states to stabilize persistent IDs and support re-identification after brief occlusion. Exact merge conditions, lifecycle thresholds, deletion rules, and the detailed re-identification score are provided in Supp. Material B. After these transitions, confirmed tracks are extracted and the representative components form the track pool used for the next frame.

## 4 Results and Analysis

### 4.1 Datasets

**WildTrack** [6]: 7 synchronized calibrated HD cameras (1920×1080, 2 fps) covering a 12×36 m outdoor area with ~20 pedestrians per frame; 400 frames total, 360/40 train/test split (90%/10%).

**MultiviewX** [11]: 6 synthetic cameras (1920×1080, 2 fps) covering a 16×25 m area with ~40 pedestrians per frame; same split.

**RadarScenes** [19]: 158 driving sequences from four 77 GHz radars (72 868 frames). Each point carries range, azimuth, Doppler velocity, and radar cross-section.

### 4.2 Evaluation Metrics

We report MOT metrics [4] (MOTA, MOTP) and identity-aware IDF1 [18] with a 1.0 m positive assignment threshold for the camera datasets. We further report GOSPA [16] ( $p=2, c=1, \alpha=2$ ), which jointly penalizes localization error, missed targets, and false alarms. For RadarScenes we report LSTQ [3]:  $\text{LSTQ} = \sqrt{S_{\text{cls}} \cdot S_{\text{assoc}}}$ .

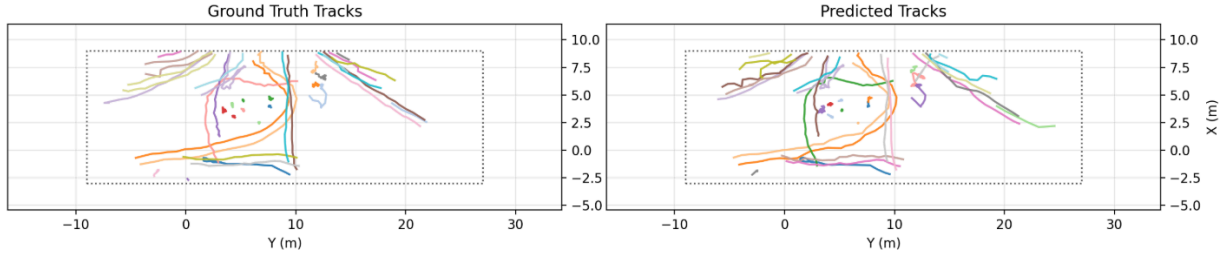


Figure 2: Predicted BEV tracks on WildTrack test set colored by identity. Ground truth (left) vs. ModTrack (right).

### 4.3 Implementation Details

YOLOv11x [12] provides monocular object detection; the Lift depth network [15] (EfficientNet-B0, 41 bins) provides an outlier check for fused geometric depth estimates; OSNet-AIN [34] trained with triplet loss via torchreid [33] provides appearance features. All perception modules are trained on the target dataset using the same 90%/10% train/test split (e.g., 360/40 frames for WildTrack); Supp. Material E summarizes the exact data preparation, losses, and optimizer settings used for the YOLO, Lift, and OSNet-AIN front-ends. All clustering, tracking, and calibration hyperparameters are detailed in Tables 6 and 7.

### 4.4 Camera Tracking Results

Figure 2 shows qualitative tracking results of ModTrack on the test set of WildTrack. Table 1 compares ModTrack against end-to-end and modular baselines on WildTrack and MultiviewX. Among modular methods, ModTrack surpasses all prior work by +21.2 IDF1 and +21.7 MOTA on WildTrack. GOSPA scores of 1.20 and 1.83 reaffirms strong tracking performance.

The best end-to-end method [27] exceeds ModTrack by 1.0 IDF1 and 2.9 MOTA on WildTrack; in exchange, ModTrack provides sensor-agnostic deployment without retraining and physically traceable uncertainty. The larger gap between ModTrack and other methods on MultiviewX (86.3 vs. 92.8 MOTA) reflects its  $2\times$  higher pedestrian density, which increases clustering ambiguity under the Euclidean gate. However, ModTrack leads all methods in IDF1 on MultiviewX, the primary tracking consistency metric, despite the higher crowd density.

**Oracle detection analysis.** To isolate the quality of the tracker backend from upstream perception noise, we replace the output of the monocular object detector with ground-truth bounding boxes; we refer to this configuration as *oracle detection*. Under oracle detection, ModTrack achieves 97.1/94.7/94.0 (IDF1/MOTA/MOTP) on WildTrack, which would be SOTA. On MultiviewX, oracle performance reaches 88.2/93.6 (IDF1/MOTA), closing the MOTA gap with end-to-end methods entirely (93.6 vs. 92.8). These results establish that the residual gap under standard operation originates entirely in the upstream perception modules. Because ModTrack’s perception modules are replaceable, improvements in detection or depth estimation directly improve tracking without modifying the tracker.

### 4.5 Ablation Studies

Table 2 compares ModTrack’s three matching modes on the two camera datasets: geometric-only association (*Spatial*), appearance-only association (*Semantic*), and the combined *Joint* configuration. Spatial-only achieves strong MOTA (89.5), confirming that calibrated geometric reasoning alone

Table 1: Multi-view pedestrian tracking on WildTrack and MultiviewX. †End-to-end methods require retraining or additional engineering accommodations to operate under sensor reconfiguration.

Method	WildTrack				MultiviewX			
	IDF1	MOTA	MOTP	GOSPA↓	IDF1	MOTA	MOTP	GOSPA↓
<i>End-to-end (fixed config.)†</i>								
EarlyBird [20]	92.3	89.5	86.6	–	82.4	88.4	86.2	–
Ali et al. [1]	92.0	87.4	–	–	–	–	–	–
MCBLT [25]	95.6	92.6	<b>94.3</b>	–	–	–	–	–
TrackTacular [21]	95.3	91.8	85.4	–	85.6	92.4	80.1	–
SCFusion [22]	95.9	92.4	86.3	–	85.0	92.5	85.4	–
Alturki et al. [2]	96.1	92.7	88.8	–	85.7	91.3	86.9	–
MVTrajecter [27]	<b>96.5</b>	<b>94.3</b>	93.0	–	<b>85.8</b>	<b>92.8</b>	<b>95.0</b>	–
<i>Learned (Non-Interpretable)</i>								
DMCT [28]	77.8	72.8	79.1	–	–	–	–	–
ReST [8]	86.7	84.9	84.1	–	–	–	–	–
UMPN [9]	96.3	93.9	86.9	–	–	–	–	–
<i>Modular (flexible config.)</i>								
KSP-DO [6]	73.2	69.6	61.5	–	–	–	–	–
MV-GLMB-OC [14]	74.3	69.7	73.2	–	–	–	–	–
<b>ModTrack (Ours)</b>	<b>95.5</b>	<b>91.4</b>	<b>87.2</b>	<b>1.20</b>	<b>86.2</b>	<b>86.3</b>	<b>84.0</b>	<b>1.83</b>
ModTrack (Oracle det.)	97.1	94.7	94.0	0.68	88.2	93.6	88.8	1.25

Table 2: Ablation of matching modes on WildTrack and MultiviewX. Joint mode uses spatial clustering and reserves semantic features for the tracking stage.

Mode	WildTrack				MultiviewX			
	IDF1	MOTA	MOTP	GOSPA	IDF1	MOTA	MOTP	GOSPA
Spatial only	86.6	89.5	82.4	1.22	84.2	84.9	83.7	1.86
Semantic only	49.6	41.8	79.6	2.60	65.1	56.7	79.6	3.00
<b>Joint (full)</b>	<b>95.5</b>	<b>91.4</b>	<b>87.2</b>	<b>1.20</b>	<b>86.2</b>	<b>86.3</b>	<b>84.0</b>	<b>1.83</b>

provides robust association. The +8.9 IDF1 improvement from joint mode on WildTrack (+2.0 on MultiviewX) comes entirely from better identity preservation through appearance-informed tracking.

#### 4.6 Deployment Robustness: Sensor Dropout and Addition

Table 3 quantifies ModTrack’s sensor dropout robustness by exhaustively evaluating all  $\binom{7}{k}$  camera subsets on WildTrack (120 configurations).

In real-world scenarios where sensor dropout or addition can happen instantaneously, our system adapts seamlessly and effectively, while end-to-end methods in Table 1 would need additional engineering accommodations or retraining. With only 5 of 7 cameras, ModTrack achieves 85.1 IDF1 and 81.1 MOTA, surpassing MV-GLMB-OC (74.3/69.7) *with all 7 cameras* by over 10 points. Additionally, MOTP remains above 80 with just 3 cameras, confirming graceful degradation across all metrics as camera coverage reduces.

Table 3: Sensor dropout robustness (WildTrack, joint mode). Mean $\pm$ std over all  $\binom{7}{k}$  subsets. GOSPA ( $p=2, c=1\text{ m}, \alpha=2$ ): lower is better.

	Cameras available					
	7	6	5	4	3	2
IDF1	95.5	91.7 $\pm$ 2.9	85.1 $\pm$ 5.3	74.5 $\pm$ 9.7	57.8 $\pm$ 15.7	31.6 $\pm$ 19.5
MOTA	91.4	87.7 $\pm$ 2.0	81.1 $\pm$ 4.7	70.2 $\pm$ 9.0	51.7 $\pm$ 16.2	25.5 $\pm$ 18.3
MOTP	87.2	85.9 $\pm$ 0.9	83.8 $\pm$ 2.9	82.4 $\pm$ 3.0	80.7 $\pm$ 4.2	73.2 $\pm$ 18.2
GOSPA	1.2	1.3 $\pm$ 0.1	1.5 $\pm$ 0.2	1.9 $\pm$ 0.3	2.3 $\pm$ 0.4	2.9 $\pm$ 0.4

Table 4: RadarScenes cross-modality validation (all 158 scenes). The tracker core is identical to Table 1; only the perception front-end differs.

Perception	LSTQ	$S_{\text{cls}}$	$S_{\text{assoc}}$
Radar Tracker (trained)	66.8	92.7	48.2
ModTrack Doppler (zero training)	42.1	70.0	26.9
ModTrack Oracle (GT labels)	76.9	99.1	60.9

The increasing standard deviation for IDF1 at lower camera counts ( $\pm 2.9$  at  $k=6$  vs.  $\pm 15.7$  at  $k=3$ ) quantifies which camera placements are critical, directly informing redundancy planning.

Figure 3 visualizes how each additional sensor contributes measurable information through precision-weighted fusion, with shrinking covariance ellipses quantifying the reduction in localization uncertainty that underlies the performance trends in Table 3.

#### 4.7 Radar Tracking Results

The  $(\mathbf{z}, R)$  interface extends naturally to any sensor producing a calibrated BEV position and covariance. We validate this by applying the identical tracker core to automotive radar on RadarScenes [19], replacing only the perception front-end (Section 3.1.2).

Table 4 shows LSTQ = 42.1 with a zero-training Doppler front-end. Replacing only the moving-object classification and object class with ground-truth labels, while retaining the noisy radar positions and covariances, raises LSTQ to 76.9 and surpasses the trained Radar Tracker [29] (66.8) by 10.1 points. The entire gap is in perception: a stronger front-end translates directly into better tracking without any changes to the tracker.

#### 4.8 Runtime Analysis

When tested on WildTrack, the tracking backend (clustering, fusion, PHD filter) accounts for less than 20% of per-frame latency (103 ms vs. 444 ms for neural perception on an NVIDIA RTX 3090 GPU); a full breakdown is provided in Supp. Material C.

#### 4.9 Sensitivity Analysis

To assess the robustness of ModTrack to hyperparameter choices, we perform a one-at-a-time sensitivity analysis on the WildTrack benchmark.

Only three parameters,  $\tau_{\text{euc}}$  (Euclidean gating),  $\tau_{\text{high}}$  (ByteTrack high confidence threshold), and  $\tau_{\text{birth}}$  (minimum cluster confidence for track birth), meaningfully affect IDF1 (Figure 4); all

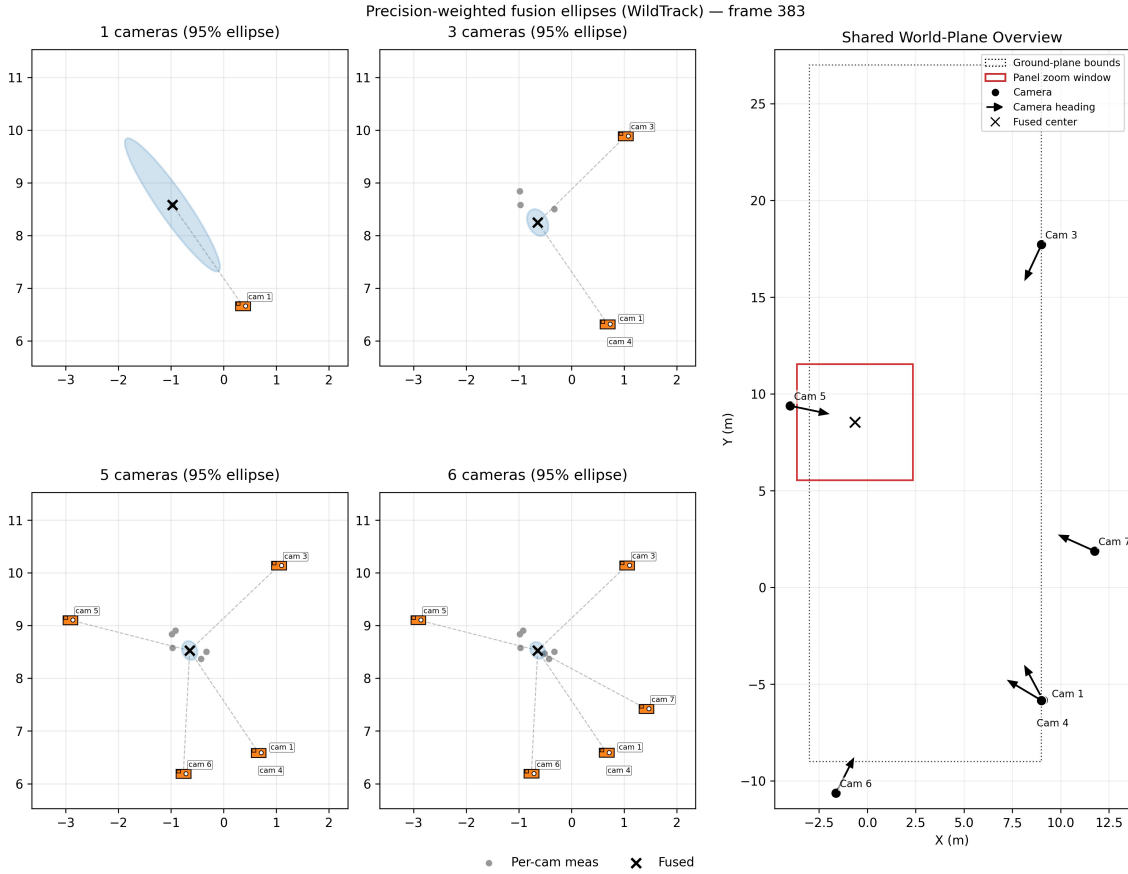
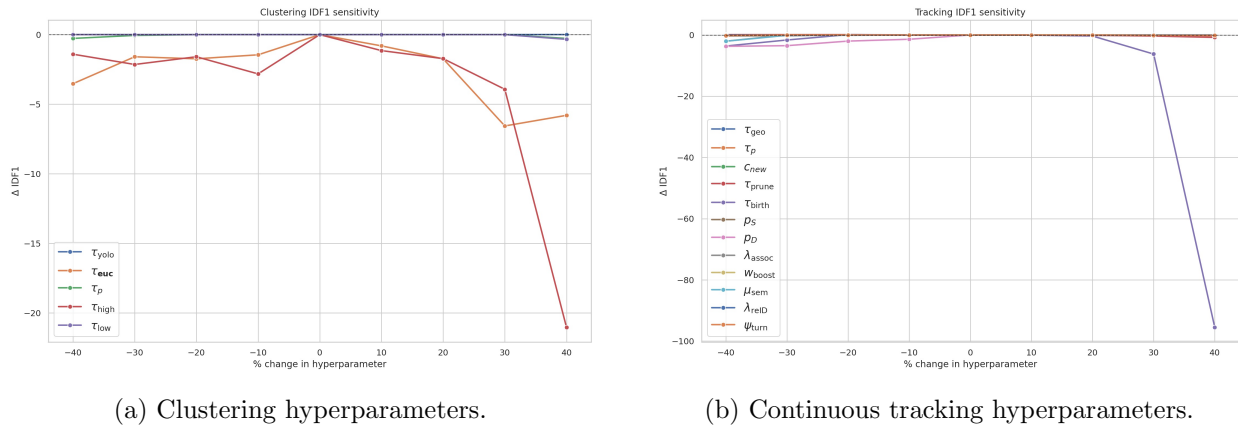


Figure 3: Precision-weighted fusion on WildTrack (frame 383). Each panel shows BEV covariance ellipses (95% confidence) as cameras are incrementally added. The rightmost panel shows the 6-camera shared world-plane.



(a) Clustering hyperparameters.

(b) Continuous tracking hyperparameters.

Figure 4: IDF1 sensitivity to hyperparameter perturbation on WildTrack (joint mode). Each parameter is swept individually; all others held at defaults. Extended results are in Supp. Material D.

three directly control the FP/FN tradeoff, and all remaining parameters vary by at most 2–3 IDF1 points.

## 5 Conclusion

ModTrack demonstrates that restricting neural networks to perception while performing downstream reasoning with closed-form analytical methods can match end-to-end performance while providing deployment flexibility, auditable uncertainty, and sensor agnosticism. Across WildTrack, MultiviewX, and RadarScenes, the same identity-informed GM-PHD tracking core operates unchanged, while the closed-loop identity mechanism and sensor-agnostic  $(\mathbf{z}, R)$  covariance chain enable robust operation under sensor dropout. Oracle detection experiments confirm that the tracker backend is not the limiting factor: with improved perception, ModTrack’s tracking performance scales directly toward SOTA. More broadly, the explicit propagation of calibrated uncertainty throughout the pipeline enables future sensor placement and selection strategies that maximize information gain in detection and tracking systems.

## References

- [1] Ali, R., Mehlretter, M., Heipke, C.: Integrating viewing direction and image features for robust multi-view multi-object 3d pedestrian tracking. *ISPRS Annals of the Photogrammetry, Remote Sensing and Spatial Information Sciences* **X-G-2025**, 47–55 (2025). <https://doi.org/10.5194/isprs-annals-X-G-2025-47-2025>
- [2] Alturki, R., Hilton, A., Guillemaut, J.Y.: Attention-aware multi-view pedestrian tracking. *arXiv preprint arXiv:2504.03047* (2025)
- [3] Aygün, M., Ošep, A., Weber, M., Maximov, M., Stachniss, C., Gall, J., Leal-Taixé, L.: 4d panoptic LiDAR segmentation. In: *Proc. IEEE/CVF Conf. Computer Vision and Pattern Recognition (CVPR)*. pp. 5527–5537 (2021)
- [4] Bernardin, K., Stiefelhagen, R.: Evaluating multiple object tracking performance: the CLEAR MOT metrics. *EURASIP Journal on Image and Video Processing* **2008**, 1–10 (2008)
- [5] Blom, H.A.P., Bar-Shalom, Y.: The interacting multiple model algorithm for systems with Markovian switching coefficients. *IEEE Trans. Automatic Control* **33**(8), 780–783 (1988)
- [6] Chavdarova, T., Baqué, P., Bouquet, S., Maksai, A., Jose, C., Bagautdinov, T., Lettry, L., Fua, P., Van Gool, L., Fleuret, F.: WildTrack: A multi-camera HD dataset for dense unscripted pedestrian detection. In: *Proc. IEEE Conf. Computer Vision and Pattern Recognition (CVPR)*. pp. 5030–5039 (2018)
- [7] Chen, L., Ai, H., Zhuang, Z., Shang, C.: Real-time multiple people tracking with deeply learned candidate selection and person re-identification. In: *Proc. IEEE Int. Conf. Multimedia and Expo (ICME)*. pp. 1–6 (2017)
- [8] Cheng, C.C., Qiu, M.X., Chiang, C.K., Lai, S.H.: ReST: A reconfigurable spatial-temporal graph model for multi-camera multi-object tracking. In: *Proc. IEEE/CVF Int. Conf. Computer Vision (ICCV)*. pp. 10051–10060 (2023)

- [9] Engilberge, M., Vrkić, I., Grosche, F.W., Pilet, J., Turetken, E., Fua, P.: One graph to track them all: Dynamic GNNs for single- and multi-view tracking. arXiv preprint arXiv:2507.08494v2 (2025)
- [10] Ester, M., Kriegel, H.P., Sander, J., Xu, X.: A density-based algorithm for discovering clusters in large spatial databases with noise. In: Proc. 2nd Int. Conf. Knowledge Discovery and Data Mining (KDD). pp. 226–231. AAAI Press (1996)
- [11] Hou, Y., Zheng, L., Gould, S.: Multiview detection with feature perspective transformation. In: ECCV (2020)
- [12] Jocher, G., Qiu, J.: Ultralytics yolo11 (2024), <https://github.com/ultralytics/ultralytics>
- [13] Kuhn, H.W.: The Hungarian method for the assignment problem. *Naval Research Logistics Quarterly* **2**(1–2), 83–97 (1955)
- [14] Ong, J., Vo, B.T., Vo, B.N., Kim, D.Y., Nordholm, S.: A Bayesian filter for multi-view 3D multi-object tracking with occlusion handling. *IEEE Trans. Pattern Analysis and Machine Intelligence* **44**(5), 2246–2263 (2022)
- [15] Phillion, J., Fidler, S.: Lift, splat, shoot: Encoding images from arbitrary camera rigs by implicitly unprojecting to 3D. In: Proc. European Conf. Computer Vision (ECCV). pp. 194–210 (2020)
- [16] Rahmathullah, A.S., García-Fernández, Á.F., Svensson, L.: Generalized optimal sub-pattern assignment metric. In: 2017 20th International Conference on Information Fusion (Fusion). pp. 1–8. IEEE (2017). <https://doi.org/10.23919/ICIF.2017.8009645>
- [17] Reuter, S., Vo, B.T., Vo, B.N., Dietmayer, K.: The labeled multi-bernoulli filter. *IEEE Transactions on Signal Processing* **62**(12), 3246–3260 (2014). <https://doi.org/10.1109/TSP.2014.2323064>
- [18] Ristani, E., Solera, F., Zou, R., Cucchiara, R., Tomasi, C.: Performance measures and a data set for multi-target, multi-camera tracking. In: Proc. European Conf. Computer Vision Workshops (ECCVW) (2016)
- [19] Schumann, O., Hahn, M., Scheiner, N., Weishaupt, F., Tilly, J.F., Dickmann, J., Wöhler, C.: RadarScenes: A real-world radar point cloud data set for automotive applications. In: Proc. 24th Int. Conf. Information Fusion (FUSION). pp. 1–8 (2021)
- [20] Teepe, T., Wolters, P., Gilg, J., Herzog, F., Rigoll, G.: EarlyBird: Early-fusion for multi-view tracking in the bird’s eye view. In: Proc. IEEE/CVF Winter Conf. Applications of Computer Vision (WACV). pp. 102–111 (2024)
- [21] Teepe, T., Wolters, P., Gilg, J., Herzog, F., Rigoll, G.: Lifting multi-view detection and tracking to the bird’s eye view. In: Proc. IEEE/CVF Conf. Computer Vision and Pattern Recognition Workshops (CVPRW) (2024)
- [22] Toida, K., Sakai, T., Kato, N., Yokota, K., Nakamura, T., Hotta, K.: Sparse bev fusion with self-view consistency for multi-view detection and tracking (2025)

- [23] Vo, B.N., Ma, W.K.: The Gaussian mixture probability hypothesis density filter. *IEEE Trans. Signal Processing* **54**(11), 4091–4104 (2006)
- [24] Vo, B.N., Vo, B.T., Phung, D.: Labeled random finite sets and the Bayes multi-target tracking filter. *IEEE Trans. Signal Processing* **62**(24), 6554–6567 (2014)
- [25] Wang, Y., Meinhardt, T., Cetintas, O., Yang, C.Y., Pusegaonkar, S.S., Missaoui, B., Biswas, S., Tang, Z., Leal-Taixé, L.: MCBLT: Multi-camera multi-object 3d tracking in long videos. In: *Proc. IEEE/CVF Conf. Computer Vision and Pattern Recognition Workshops (CVPRW)* (2025)
- [26] Wei, L., Zhang, S., Gao, W., Tian, Q.: Person transfer GAN to bridge domain gap for person re-identification. In: *Proc. IEEE/CVF Conf. Computer Vision and Pattern Recognition (CVPR)*. pp. 79–88 (2018)
- [27] Yamane, T., Masumura, R., Suzuki, S., Orihashi, S.: MVTrajecter: Multi-view pedestrian tracking with trajectory motion cost and trajectory appearance cost. In: *Proc. IEEE/CVF Int. Conf. Computer Vision (ICCV)* (2025)
- [28] You, Q., Jiang, H.: Real-time 3D deep multi-camera tracking. *arXiv preprint arXiv:2003.11753* (2020)
- [29] Zeller, M., Casado Herraiz, D., Behley, J., Heidingsfeld, M., Stachniss, C.: Radar tracker: Moving instance tracking in sparse and noisy radar point clouds. In: *Proc. IEEE Int. Conf. Robotics and Automation (ICRA)* (2024)
- [30] Zhang, Y., Sun, P., Jiang, Y., Yu, D., Weng, F., Yuan, Z., Luo, P., Liu, W., Wang, X.: ByteTrack: Multi-object tracking by associating every detection box. In: *Proc. European Conf. Computer Vision (ECCV)*. pp. 1–21 (2022)
- [31] Zhang, Y., Zheng, Z., Liu, J., Huang, Z., Zhou, Z., Meng, Z., Cai, T., Ma, J.: Mic-bev: Multi-infrastructure camera bird’s-eye-view transformer with relation-aware fusion for 3d object detection (2025), <https://arxiv.org/abs/2510.24688>
- [32] Zheng, L., Shen, L., Tian, L., Wang, S., Wang, J., Tian, Q.: Scalable person re-identification: A benchmark. In: *Proc. IEEE Int. Conf. Computer Vision (ICCV)*. pp. 1116–1124 (2015)
- [33] Zhou, K., Xiang, T.: Torchreid: A library for deep learning person re-identification in Pytorch. *arXiv preprint arXiv:1910.10093* (2019)
- [34] Zhou, K., Yang, Y., Cavallaro, A., Xiang, T.: Learning generalisable omni-scale representations for person re-identification. *IEEE Trans. Pattern Analysis and Machine Intelligence* **44**(9), 5056–5069 (2022)

## A Depth Estimation Details

**Planar footpoint projection.** The bottom-center pixel  $(u_f, v_f)$  of each bounding box is back-projected using camera intrinsics  $K$  to obtain the normalized camera-frame ray

$$\mathbf{r}_c = K^{-1}[u_f, v_f, 1]^\top.$$

Assuming a known ground plane  $\mathbf{n}^\top \mathbf{X}_w = d_{\text{plane}}$  and camera-to-world extrinsics  $(R_c, \mathbf{t}_c)$ , the signed ray-plane intersection parameter is

$$\lambda_{\text{fp}} = \frac{d_{\text{plane}} - \mathbf{n}^\top \mathbf{t}_c}{\mathbf{n}^\top (R_c \mathbf{r}_c)}.$$

We define the world/BEV frame so the ground plane is horizontal, i.e.,  $\mathbf{n} = [0, 0, 1]^\top$  and  $\mathbf{n}^\top \mathbf{X}_w = z_w = d_{\text{plane}}$ . Thus, the orthogonal projection in Section 3.2 changes only  $z_w$ , so Equation (26) needs no additional in-plane projection factor.

We define the metric depth estimate as

$$d_{\text{fp}} = |\lambda_{\text{fp}}|, \quad \sigma_{\text{fp}}^2 = \max((\alpha_{fp} d_{\text{fp}})^2, \sigma_{\text{min depth}}^2), \quad (21)$$

where  $\alpha_{fp} = 0.035$  controls relative geometric uncertainty.

**Bounding-box depth prior.** A complementary estimate follows from the observed bounding-box height  $h_{\text{px}}$  under the pinhole model with vertical focal length  $f_y$  and reference object height  $H_{\text{ref}}$ :

$$d_{\text{bbox}} = \frac{f_y H_{\text{ref}}}{h_{\text{px}}}, \quad \sigma_{\text{bbox}}^2 = \max((\alpha_{bbox} d_{\text{bbox}})^2, \sigma_{\text{min depth}}^2), \quad (22)$$

where  $\alpha_{bbox} = 0.05$  controls the relative bounding-box uncertainty.

**Fused depth estimate.** The two geometric cues are combined via precision weighting:

$$\hat{d} = \frac{\pi_{\text{fp}} d_{\text{fp}} + \pi_{\text{bbox}} d_{\text{bbox}}}{\pi_{\text{fp}} + \pi_{\text{bbox}}}, \quad \pi_{\text{fp}} = \frac{\eta_{\text{fp}}}{\sigma_{\text{fp}}^2}, \quad \pi_{\text{bbox}} = \frac{1}{\sigma_{\text{bbox}}^2}, \quad (23)$$

where  $\eta_{\text{fp}} = 3$  reflects the lower systematic bias of the ground-plane cue. Depth uncertainty is parameterized as

$$\sigma_d^2 = \max((\alpha_{fp} |\hat{d}|)^2, \sigma_{\text{min depth}}^2).$$

Finally, a Lift-style depth network [15] is used as an outlier check: if its predicted depth differs from  $|\hat{d}|$  by more than 3m while indicating high confidence, the variance is inflated by  $\gamma_{\text{inflate}} = 1.75$ .

## A.1 BEV Projection and Covariance Propagation

Section 3.2 gives the operational summary; here we provide the full projection and covariance derivation used for camera measurements.

Given a detection at pixel  $(u, v)$  in camera  $c$ , we back-project  $\mathbf{r}_c = K^{-1}[u, v, 1]^\top$  and form the world point

$$\mathbf{X}_w = R_c (\hat{d} \mathbf{r}_c) + \mathbf{t}_c. \quad (24)$$

To enforce a ground-plane measurement, we orthogonally project onto  $\mathbf{n}^\top \mathbf{X} = d_{\text{plane}}$ :

$$\mathbf{X}_{\text{proj}} = \mathbf{X}_w + (d_{\text{plane}} - \mathbf{n}^\top \mathbf{X}_w) \mathbf{n}, \quad (25)$$

and define the BEV position  $\mathbf{z}_{\text{BEV}} = \mathbf{X}_{\text{proj}, 1:2}$ .

Holding  $(u, v)$  fixed, the full derivative through the plane projection is  $(I - \mathbf{nn}^\top) R_c \mathbf{r}_c$ ; since we define  $\mathbf{n} = [0, 0, 1]^\top$  (horizontal ground plane, see Section A), the projector  $(I - \mathbf{nn}^\top) = \text{diag}(1, 1, 0)$  affects only the vertical component, so extracting rows 1:2 gives the Jacobian

$$J = \frac{\partial \mathbf{z}_{\text{BEV}}}{\partial \hat{d}} = R_{c, 1:2, :} K^{-1} \begin{bmatrix} u \\ v \\ 1 \end{bmatrix} \in \mathbb{R}^{2 \times 1}. \quad (26)$$

Propagating depth uncertainty yields the rank-1 BEV covariance term

$$R_{\text{depth}} = \sigma_d^2 J J^\top.$$

We then add the isotropic pose/calibration term

$$R_{\text{pose}} = \sigma_{\text{pose}}^2 I_2.$$

To preserve a minimum eigenvalue  $\sigma_{\text{min}}^2$  for the final BEV covariance, we floor only the independent depth term before adding  $R_{\text{pose}}$ . With  $\lambda_{\text{min}}(R_{\text{pose}})$  the smallest eigenvalue of  $R_{\text{pose}}$ , we set

$$\sigma_{\text{min,indep}}^2 = \max(0, \sigma_{\text{min}}^2 - \lambda_{\text{min}}(R_{\text{pose}})), \quad (27)$$

and clamp the eigenvalues of  $R_{\text{depth}}$  to be at least  $\sigma_{\text{min,indep}}^2$ . The final measurement covariance is

$$R_{\text{BEV}} = R_{\text{depth}} + R_{\text{pose}}.$$

## B Full Identity-Informed GM-PHD Details

### B.1 Association and Update Details

**Track-level grouping.** Components are grouped by identity; for each track  $t$  and measurement  $i$ , the grouped cost is  $c_{t,i} = \min_{j \in \mathcal{J}_k(t)} c_{ij}$ . Collecting these entries yields the track-level cost matrix  $C_{\text{track}} = [c_{t,i}]$ .

Dedicated miss columns with cost  $= -\log(1 - p_D^{(c)})$  allow tracks to remain unmatched:

$$C_{\text{full}} = [C_{\text{track}} \mid \text{diag}(-\log(1 - p_D^{(c)}))]. \quad (28)$$

Hungarian assignment on  $C_{\text{full}}$  yields globally optimal 1:1 track-to-measurement matching.

We apply Equation (28) only to CONFIRMED tracks to avoid weight dilution in dense scenes. Remaining TENTATIVE/LOST tracks are then processed in a second pass using only measurements not claimed by the confirmed-track Hungarian: we accumulate soft association evidence over  $\chi_2^2$ -gated pairs (using  $d_{ij}^2$  from Equation (16)) and apply the Kalman update in Equation (20) only for a best match that satisfies a tighter gate ( $\chi_{2,0.90}^2 = 4.61$ ). For LOST tracks, we additionally boost re-identification using appearance similarity as in Section 3.5.5.

### B.2 Component Management and Lifecycle Details

After the PHD update, component management is applied before any tracks are exposed externally. Low-weight components are pruned first, then components with identical identities and small Mahalanobis distance ( $< \tau_{\text{merge}}$ ) are merged via moment matching, and we finally retain only the highest-weight motion-mode component per identity, yielding one representative component (track state) per persistent ID for lifecycle handling and next-frame association.

Tracks follow a three-state lifecycle: TENTATIVE  $\rightarrow$  CONFIRMED (after  $N_{\text{init}}$  hits or deleted if misses exceed  $\tau_{\text{tent}}$ )  $\rightarrow$  LOST (after  $\tau_{\text{confirmed}}$  consecutive misses), with deletion after age  $K_{\text{max}}$  without re-association. Hit counters decay gradually ( $h \leftarrow \max(0, h-1)$ ) rather than resetting on a miss, preserving accumulated evidence. Re-identification of lost tracks uses a combined spatial-semantic score:  $\text{score}(i, j) = -d_{\text{Mahal}}^2 + \lambda_{\text{reID}} \cdot \cos(\mathbf{f}_{\text{lost}}, \mathbf{f}_{\text{meas}})$ .

Table 5: Per-frame inference time breakdown on WildTrack (7 cameras, RTX 3090). The analytical core accounts for less than 20% of total latency; perception dominates runtime.

Stage	Time (ms)	% Total	FPS
Neural perception (Det. + Depth + Feat.)	443.9	81.0	2.25
Analytical core (Clust. + Fusion + PHD)	103.2	18.8	9.69
Other overhead	0.7	0.1	–
<b>ModTrack (Total)</b>	<b>547.8 ± 85.0</b>	<b>100</b>	<b>1.83</b>

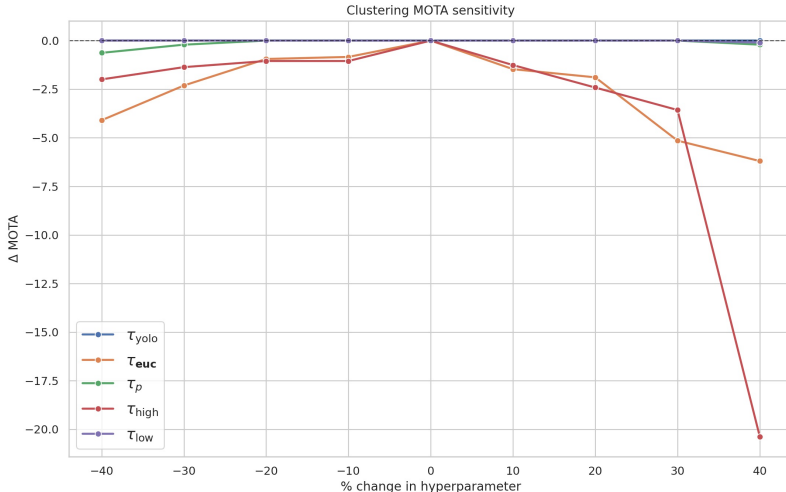


Figure 5: MOTA sensitivity to continuous clustering hyperparameters on WildTrack.

## C Runtime Analysis

Table 5 reports per-frame timing on WildTrack (RTX 3090), averaged after skipping five warm-up frames.

## D Extended Sensitivity Analysis

This appendix provides additional sensitivity results beyond the clustering and continuous tracking sweeps shown in Figure 4. Each hyperparameter is swept while all others are held at their default values.

**Clustering parameters** (Figures 4a, 5 and 6).

**Tracking parameters** (Figures 7 to 11).  $N_{init}$  (hits required for confirmation) and  $\tau_{confirmed}$  (misses before entering lost state) show moderate sensitivity but only to the effect of  $\sim 2\text{--}3$  percentage points of IDF1.  $K_{max}$  (maximum lost age before deletion) is largely insensitive and  $\tau_{tent}$  has no effect within the tested range.

**Calibration parameters** (Figures 12 to 14). All calibration parameters show minimal sensitivity in the range of 1.2 points of IDF1, 1.0 points of MOTA, and 0.0025 points of MOTP.

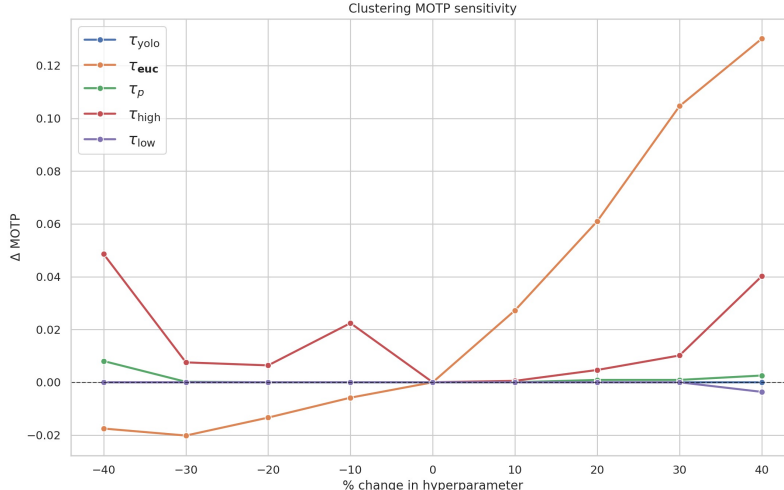


Figure 6: MOTP sensitivity to continuous clustering hyperparameters on WildTrack.

## E Camera Perception Training Details

All three learned front-ends are trained independently on a single NVIDIA RTX 3090 GPU using the same ordered 90/10 frame split in the main experiments for WildTrack and MultiviewX. This keeps the perception stack aligned with the tracker evaluation split while avoiding frame-level leakage across time.

### E.1 YOLOv11x Detector Fine-Tuning

The YOLO model is fine-tuned with the standard YOLO training pipeline maintained by Ultralytics [12], using `imgsz=640` so the network sees a consistent square training resolution. We initialize from a pretrained YOLOv11x checkpoint, train for 50 epochs with batch size 8. After training, the best validation checkpoint is retained as the dataset-specific detector weights.

### E.2 Lift Depth Network Training

Ground truth for the depth model is obtained by assigning the annotated 3D person location to every pixel within its corresponding ground-truth 2D box, yielding sparse but geometrically exact supervision. The CamEncode network is initialized from the released LSS checkpoint, uses 41 linear depth bins over  $[1, 36]$  m, a context dimension of 64, and  $360 \times 640$  RGB inputs; images are scaled to  $[0, 1]$  and normalized with ImageNet mean/std to match the EfficientNet-B0 backbone initialization. Training runs for 50 epochs with batch size 8 using AdamW, learning rate  $10^{-4}$ , weight decay  $10^{-4}$ , and gradient clipping at 1.0. During training the model predicts depth logits over the full image, for each ground truth box a Gaussian centered in the box is used to sample  $n = 16$  points, the expected depth is computed from the predicted sampled depth logits, and an  $L_1$  loss is applied against the box’s ground truth metric depth. The checkpoint with the lowest validation  $L_1$  error is retained as the final Lift model.

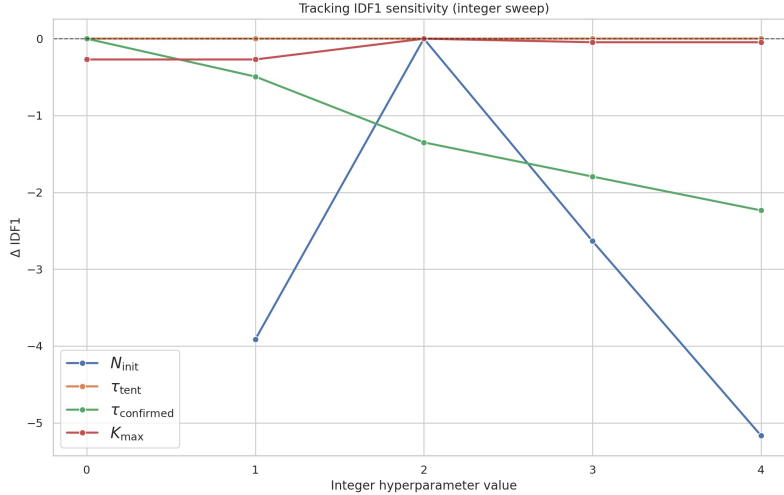


Figure 7: IDF1 sensitivity to integer tracking hyperparameters ( $N_{\text{init}}$ ,  $\tau_{\text{tent}}$ ,  $\tau_{\text{confirmed}}$ ,  $K_{\text{max}}$ ) on WildTrack.

### E.3 OSNet-AIN ReID Training

The appearance encoder is trained on cropped person patches organized by identity and camera. Only identities observed in at least two cameras are retained so the learned embedding is explicitly cross-view. Training uses a PK sampler: with the default batch size of 64, each mini-batch contains 16 identities and four images per identity. Images are resized to  $256 \times 128$  and augmented with padding, random crop, horizontal flip, color jitter, normalization, and random erasing. OSNet-AIN is trained with batch-hard triplet loss (margin 0.3). We train for 150 epochs and 350 PK batches per epoch using AdamW (learning rate  $3 \times 10^{-4}$ , weight decay  $5 \times 10^{-4}$ ), cosine annealing to  $10^{-6}$ , and gradient clipping at 5.0. Model selection is based on the validation *pair-gap* statistic, i.e., the mean separation between same-identity and different-identity cosine-similarity rates across the chosen thresholds, and the checkpoint with the highest pair-gap is used at inference time.

## F Hyperparameter Summary

Tables 6 and 7 provide a comprehensive reference for all hyperparameters used in ModTrack across all three datasets. Camera-specific perception parameters (top block of Table 6) do not apply to RadarScenes, which instead uses the radar-specific parameters listed below them. All clustering, fusion, and tracking parameters (bottom blocks) apply to every dataset, with only numerical values differing.

## G Uncertainty Calibration Analysis

We evaluate the statistical calibration of ModTrack’s reported BEV state covariances using the Normalized Estimation Error Squared (NEES). For each frame, predicted tracks are matched to ground truth via Hungarian assignment under a 1.0 m gating threshold. Calibration is therefore evaluated *conditioned on successful associations*.

For each matched pair, we compute

$$\text{NEES} = e^\top P^{-1} e,$$

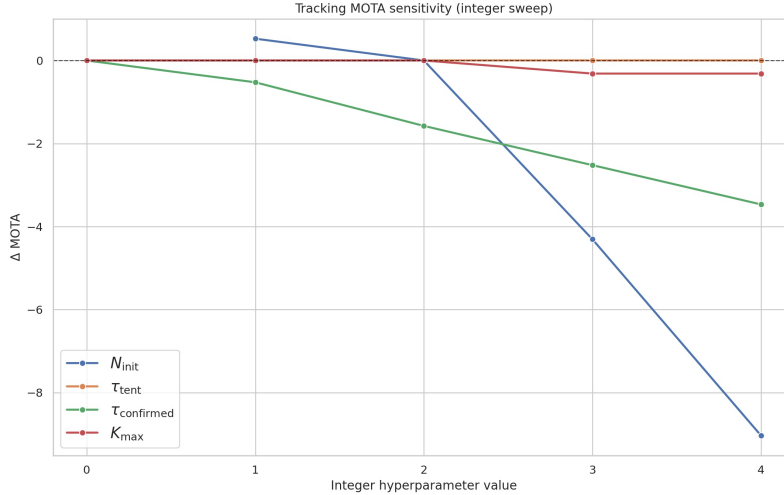


Figure 8: MOTA sensitivity to integer tracking hyperparameters ( $N_{\text{init}}$ ,  $\tau_{\text{tent}}$ ,  $\tau_{\text{confirmed}}$ ,  $K_{\text{max}}$ ) on WildTrack.

where  $e = \mathbf{z}_{gt} - \mathbf{z}_{pred}$  and  $P$  is the predicted  $2 \times 2$  position covariance. Under correct calibration,  $\mathbb{E}[\text{NEES}] = 2$  and NEES follows a  $\chi^2(2)$  distribution.

**Primary test (mean NEES).** Let  $N$  be the number of matched samples. Under the null hypothesis of correct calibration, the mean NEES lies within

$$\left[ \frac{\chi_{2N, 0.025}^2}{N}, \frac{\chi_{2N, 0.975}^2}{N} \right].$$

We classify uncertainty as: **CALIBRATED** (mean within CI), **OVERCONFIDENT** (mean above CI), or **CONSERVATIVE** (mean below CI).

**Coverage diagnostics.** In addition to the mean NEES test, we report empirical  $1\sigma$  and  $2\sigma$  coverage. For a 2D Gaussian state, a prediction is inside the  $k\sigma$  ellipse if  $\text{NEES} \leq k^2$ . Under correct calibration, the expected coverage is  $\mathbb{P}(\chi_2^2 \leq k^2)$ , which equals 39.3% for  $k = 1$  and 86.5% for  $k = 2$ .

**Interpretation.** On both datasets, mean NEES lies significantly below the theoretical expectation of 2.0, and empirical coverage exceeds nominal  $\chi^2$  expectations (39.3% for  $1\sigma$ , 86.5% for  $2\sigma$ ). This indicates that ModTrack’s propagated covariances are *conservative*, i.e., slightly overdispersed relative to empirical localization error. Importantly, no evidence of overconfidence is observed. The consistent behavior across datasets suggests that the analytical covariance propagation and precision-weighted fusion yield stable, auditable uncertainty estimates.

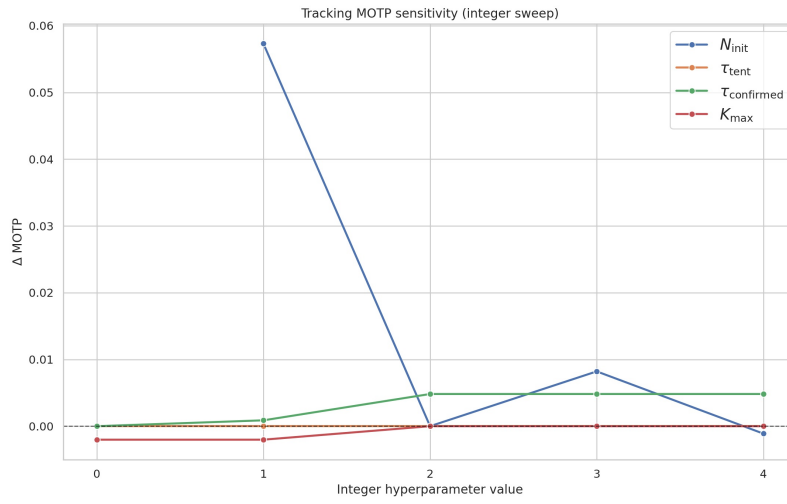


Figure 9: MOTP sensitivity to integer tracking hyperparameters ( $N_{\text{init}}$ ,  $\tau_{\text{tent}}$ ,  $\tau_{\text{confirmed}}$ ,  $K_{\text{max}}$ ) on WildTrack.

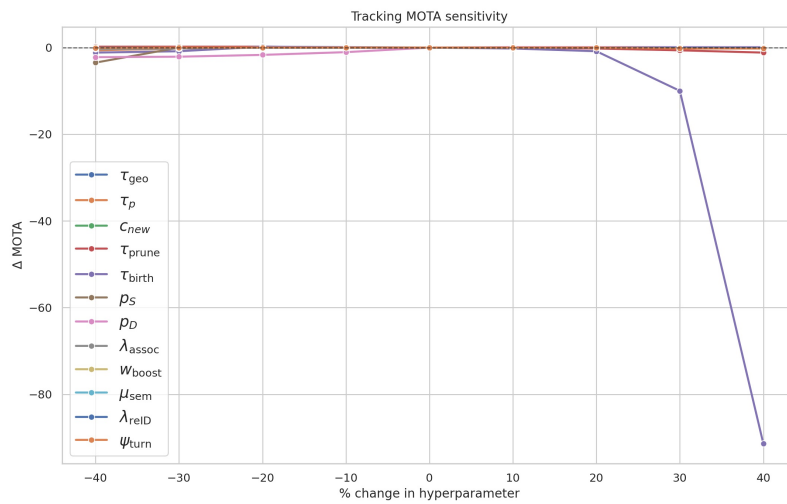


Figure 10: MOTA sensitivity to continuous tracking hyperparameters on WildTrack.

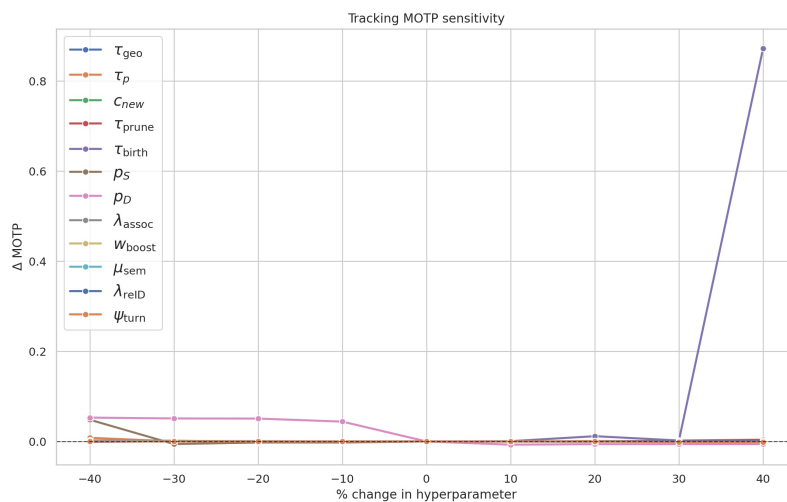


Figure 11: MOTP sensitivity to continuous tracking hyperparameters on WildTrack.

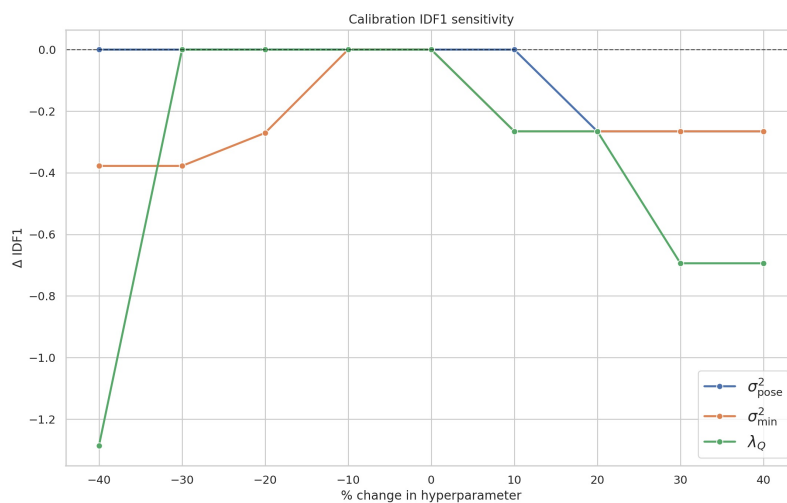


Figure 12: IDF1 sensitivity to calibration hyperparameters ( $\sigma_{pose}^2$ ,  $\sigma_{min}^2$ ,  $\lambda_Q$ ) on WildTrack.

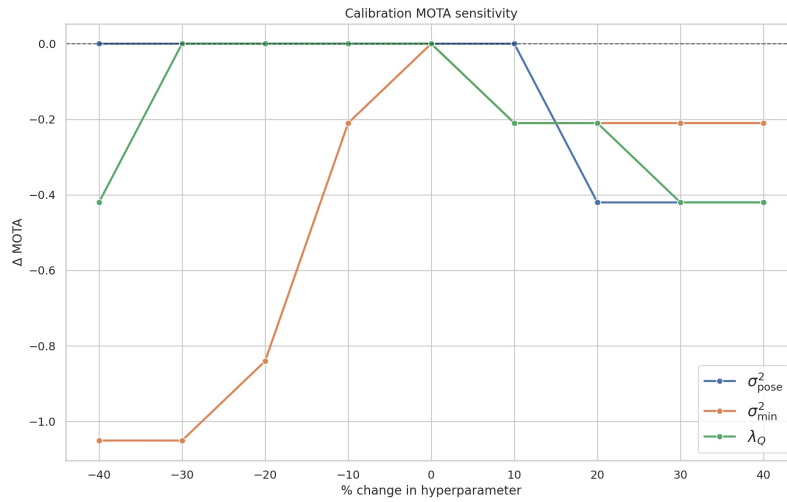


Figure 13: MOTA sensitivity to calibration hyperparameters ( $\sigma_{\text{pose}}^2$ ,  $\sigma_{\text{min}}^2$ ,  $\lambda_Q$ ) on WildTrack.

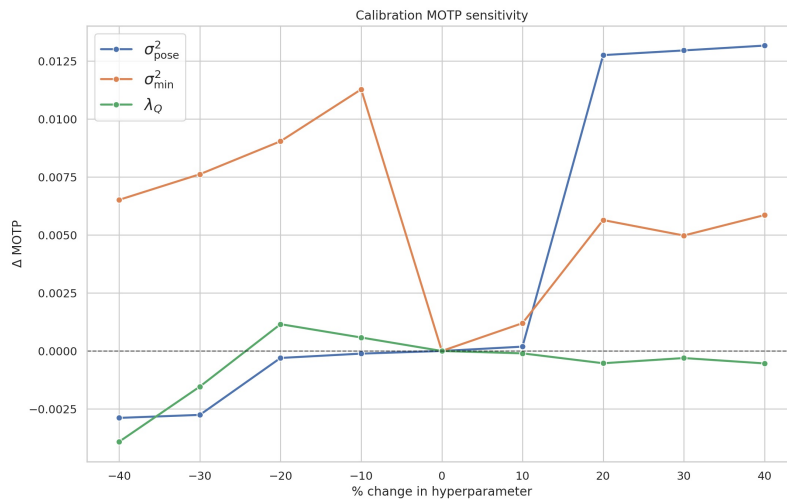


Figure 14: MOTP sensitivity to calibration hyperparameters ( $\sigma_{\text{pose}}^2$ ,  $\sigma_{\text{min}}^2$ ,  $\lambda_Q$ ) on WildTrack.

Table 6: Hyperparameters: perception, projection, and clustering stages. Camera-specific parameters (top block) do not apply to RadarScenes.

Stage	Symbol	WildTrack	MultiviewX	RadarScenes	Physical Interpretation
<i>Camera Perception</i>					
	$\tau_{\text{yolo}}$	0.1	0.63	–	Min. detector confidence to retain a detection
	$\alpha_{fp}$	0.035	0.035	–	Footpoint depth uncertainty scaling factor
	$\alpha_{bbox}$	0.05	0.05	–	Bbox depth uncertainty scaling factor
	$\eta_{fp}$	3	3	–	Footpoint precision boost (trust factor)
	$\sigma_{\text{min depth}}^2$	0.0001	0.0001	–	Min. depth variance
	$\gamma_{\text{inflate}}$	1.75	1.75	–	Variance inflation when Lift disagrees
<i>Radar Perception</i>					
	$\sigma_r$	–	–	0.10 m	Range measurement std. dev.
	$\sigma_\theta$	–	–	1.8°	Azimuth measurement std. dev.
	$\epsilon_{\text{DBSCAN}}$	–	–	2.5 m	DBSCAN neighborhood radius
	$n_{\text{min}}$	–	–	2	DBSCAN min. samples per cluster
	$v_{\text{min}}$	–	–	0.5 m/s	Min. Doppler speed (moving-object filter)
<i>BEV Projection</i>					
	$\sigma_{\text{pose}}$	0.17 m	0.22 m	0.32 m	Calibration/ego-pose uncertainty ( $\sqrt{R_{\text{pose}}}$ )
	$\sigma_{\text{min}}^2$	0.16 m <sup>2</sup>	0.21 m <sup>2</sup>	0.21 m <sup>2</sup>	Min. eigenvalue floor on BEV covariance
<i>Clustering</i>					
	$\chi^2$ gate	9.21	9.21	13.82	$\chi_2^2$ quantile (99% camera, 99.9% radar)
	$\tau_{\text{euc}}$	0.5 m	0.5 m	0.5 m	Hard Euclidean cutoff to prevent chain effects
	$\tau_{\text{high}}$	0.5	0.63	–	ByteTrack high-confidence threshold
	$\tau_{\text{low}}$	0.2	–	–	ByteTrack low-confidence threshold

Table 7: Hyperparameters: tracking, lifecycle, and motion model stages. RadarScenes uses the same GM-PHD tracking loop with dataset-specific tuning.

Stage	Symbol	WildTrack	MultiviewX	RadarScenes	Physical Interpretation
<i>Tracking (GM-PHD)</i>					
	$p_S$	0.99	0.99	0.99	Target survival probability
	$p_D$	0.90	0.95	0.90	Detection probability
	$\lambda_{\text{assoc}}$	2.5	2.5	2.5	Identity score boost in assignment cost
	$\mu_{\text{sem}}$	2.0	2.0	0.0	Appearance similarity boost (spatial-only for radar)
	$\lambda_{\text{ReID}}$	3.0	3.0	0.0	Appearance boost for LOST-track re-identification
	$w_{\text{boost}}$	0.15	0.15	0.15	Weight boost for matched components
	$\sigma_{\text{spatial}}$	1.0	1.0	1.0	Spatial bandwidth for identity kernel
	$\tau_{\text{geo}}$	5.0	5.0	5.0	Softmax temperature for identity score
	$\tau_{\text{new}}$	12.0	12.0	12.0	Cost of spawning new identity in front-end Hungarian
	$\sigma_v^{(c)}$	1.0 m/s	1.0 m/s	8.0 m/s	Birth velocity prior std. dev.
	$\tau_{\text{birth}}$	0.65	0.65	0.40	Min. cluster confidence for track birth
	$Q_{\text{scale}}$	0.9	0.9	15.0	Process noise scaling factor
<i>Track Lifecycle</i>					
	$N_{\text{init}}$	2	2	2	Hits to confirm a tentative track
	$K_{\text{max}}$	2	2	5	Max. lost age before deletion
	$J_{\text{max}}$	100	100	100	Max. mixture components retained after capping
	$\tau_{\text{confirmed}}$	0	1	3	Consecutive misses before entering lost state
	$\tau_{\text{tent}}$	1	0	2	Consecutive tentative misses before deletion
	$\tau_{\text{prune}}$	0.05	0.05	0.05	Min. component weight during pruning
	$\tau_{\text{merge}}$	2.5	2.5	2.5	Mahalanobis threshold for merging components
<i>HMM Motion Modes</i>					
	$\pi_{\text{stay}}^{(1)}$	0.75	0.75	0.70	Stationary mode self-transition prob.
	$\pi_{\text{stay}}^{(2)}$	0.94	0.94	0.95	Constant-velocity mode self-transition prob.
	$\pi_{\text{stay}}^{(3)}$	0.10	0.10	0.15	Maneuvering mode self-transition prob.
	$\Delta t$	0.5 s	0.5 s	0.2 s	Time step between frames
<i>Turn Penalty (<math>\psi_{\text{turn}}</math>)</i>					
	Speed-adaptive penalty: $\psi_{\text{turn}}(j, i) = \lambda_{\text{turn}} \cdot \ \dot{\mathbf{x}}_k^{(j)}\  \cdot (1 - \cos \Delta\theta_{ji})$ , where $\Delta\theta_{ji}$ is the angle between predicted velocity and measurement direction, and $\lambda_{\text{turn}} = 1.5$ . Penalizes sharp turns proportionally to speed.				
<i>RadarScenes Post-Processing</i>					
	$d_{\text{merge}}$	–	–	6.0 m	Tube merging max distance
	$g_{\text{merge}}$	–	–	5	Tube merging max frame gap

Table 8: Calibration statistics (matched track/GT pairs only).

Dataset	$N$	Mean NEES	95% CI	$1\sigma$ Cov.	$2\sigma$ Cov.
WildTrack	879	0.46	1.87-2.13	88.4%	98.6%
MultiviewX	1317	0.38	1.89-2.11	91.9%	99.6%